RADIO SCIENCE, VOL. 48, 265–273, doi:10.1002/rds.20027, 2013

Effects of slightly rough surfaces on the brightness temperature of the lunar regolith

Ping Chen,[1] Ping Huang,[1] Yanchun He,[1] Congcong Wang,[1] Qingxia Li,[1] Liangqi Gui,[1] Quanliang Huang,[1] Liang Lang,[1] Yongchun Zheng,[2] Xiongyao Li,[3] and Lei Hua[1]

Received 4 June 2012; revised 22 February 2013; accepted 5 March 2013; published 19 June 2013.

[1] *Keihm* [1984] made a study on the effects of the rough lunar surface on microwave brightness temperature using geometric optics (GO), which is valid only when the microwave wavelength is much smaller than the radius of curvature of the rough surface. This approach is deficient because it has no explicit wavelength dependence. The Chang'E-1 Lunar Orbiter carried out lunar microwave remote sensing of maria where the surface can be regarded as "slightly" rough, and this has motivated our study. We model the mare regolith as a multilayer planar layered media with a slightly rough top surface, and the temperature profile is retrieved by solving the heat conduction equation. The noncoherent method is utilized to calculate the emission of the multilayer media. To calculate the effect of the rough top surface on brightness temperatures, we use the bistatic transmission coefficients by applying the second-order small perturbation method. Using this model, the microwave brightness temperatures of the Apollo 12 area under different roughness conditions are calculated. It is shown that a slightly rough surface will increase or decrease the microwave radiative brightness temperature of the lunar regolith and that the change is related to the roughness, incidence angle, frequency, and polarization. In the case of measurements made by the Chang'E-1 microwave radiometer, where the incidence angle is 0°, the small-scale roughness will increase the brightness temperature of the lunar regolith.

Citation: Chen, P., P. Huang, Y. He, C. Wang, Q. Li, L. Gui, Q. Huang, L. Lang, Y. Zheng, X. Li, and L. Hua (2013), Effects of slightly rough surfaces on the brightness temperature of the lunar regolith, *Radio Sci.*, *48*, 265–273, doi:10.1002/rds.20027.

1. Introduction

[2] One of the scientific goals of the Chang'E-1 Lunar Orbiter (CE-1) is detecting the thickness of the lunar regolith [*Ouyang*, 2005] and estimating the reserves of helium-3, an important nuclear fuel for fission reactors. To recover the lunar regolith depth from the TBs of the multichannel microwave radiometer at 3.0, 7.8, 19.35, and 37 GHz aboard CE-1, an accurate forward model for the TBs of the lunar surface is needed.

[3] In the existing emission models for lunar regolith [*Fa and Jin*, 2007a, 2007b, 2011; *Meng et al*., 2008; *Wang et al*., 2008], many factors influencing the TBs are considered, such as the regolith layer thickness, the temperature profile, the lunar soil bulk density, and the dielectric permittivity profiles. Usually, the regolith is modeled to a layered medium with plane interfaces [*Fa and Jin*, 2007a, 2007b, 2011; *Meng et al*., 2008; *Wang et al*., 2008]. Coherent or noncoherent radiative transfer models are used to calculate the TBs of the layered medium. A coherent radiative transfer method is suitable for the rigorous stratified medium in practice, where both amplitudes and phases of the electromagnetic waves are considered. Moreover, the results calculated by the coherent method are easily influenced by the layer thickness. Another method, i.e., the noncoherent method, ignores the influence of the phases of the waves. It is established on the premise that there are a lot of scatterers, whose scales are comparable to the wavelength of the electromagnetic wave. For lunar soil, since the dielectric constant continuously varies with depth, that is, the regolith is not the rigorous stratified medium, and virtually many scatterers with different scales are involved in the regolith, then the noncoherent method is more suitable for calculating the TBs. It is noted that all the models above assume a plane surface for the lunar regolith.

[4] However, as we know, there are undulating terrains in the range of 35–50 km, which are spatial resolutions of multichannel microwave radiometers. The undulating terrains can be regarded as a large-scale roughness. Besides, there is also a small-scale roughness on the lunar surface. Based on the analysis of the sample from Apollo 12 [*Helfenstein and Shepard*, 1999], the surface RMS height deviation h is around 0.9–3.6 mm, and the RMS slope angle θ at 1 mm scale varies

[1]Science and Technology on Multi-spectral Information Processing Laboratory, Department of Electronics and Information Engineering, Huazhong University of Science and Technology, Wuhan, China.
[2]National Astronomical Observatories, Chinese Academy of Science, Beijing, China.
[3]Institute of Geochemistry, Chinese Academy of Science, Guiyang, China.

Corresponding author: L. Gui, Science and Technology on Multi-spectral Information Processing Laboratory, Department of Electronics and Information Engineering, Huazhong University of Science and Technology, Wuhan 430074, China. (guilq@hust.edu.cn)

0048-6604/13/10.1002/rds.20027

in 13.9°–37°. The surface with this slight roughness cannot be regarded as a plane at the frequency range of the CE-1 multichannel microwave radiometer, i.e., 3–37 GHz. Therefore, it is also necessary to study the influence of the small-scale roughness on the TBs of the lunar regolith.

[5] Some studies have been made to evaluate the effect of large-scale roughness on the lunar TB. To calculate infrared emission of the Moon [*Smith*, 1967], the lunar surface is divided into many plane elements; each of them is assumed to be a perfect Lambertian emitter of thermal radiation at the infrared frequency. Then, a self-shadowing theory of rough surfaces is combined into studying infrared TBs of the Moon. *Golden* [1979] applied the Monte Carlo technique to calculate the transmission of microwave radiation through a planetary surface, which is considered to be composed of a large number of plane facets, their dimensions being assumed to be much greater than the wavelength. As shown by *Keihm* [1984], topographic effects are considered both thermal and emissive. For roughness whose scale is assumed to be characterized by slowly varying undulations with a horizontal scale that is large compared to the wavelength, a statistical geometric optics (GO) approach is employed. To study the influence of the terrains on the microwave TBs shown by *Jin and Fa* [2011], the undulating surface is divided into discrete triangular meshes, whose dimensions are 10 m. Also, the surface of each mesh is regarded as a plane. The results show that in the regions of spatial resolutions of the multichannel microwave radiometer, the effects of the terrains on the emission can be neglected. It is noted that the effect of the terrain on the temperature is not included in their study.

[6] A theory which is developed for thermal microwave emission from a homogeneous layer with rough surfaces containing spherical scatterers is shown by *Shin and Kong* [1982]. To model rough top and bottom interfaces, they use the bistatic coefficients by GO. In addition, microwave emission from a layered medium with the top interface being a rough surface is studied by the method of moments [*Tsang et al*., 2008].

[7] All the mentioned methods used for studying the lunar roughness effect are based on Kirchhoff approximation or GO, which are valid only when the microwave wavelength is much smaller than the radius of curvature of the rough surface. A defect of the simple GO model is the absence of explicit wavelength dependence; moreover, GO is not valid for the small-scale roughness described above, where the standard deviation of the local lunar surface is much smaller than the wavelength. Then, the effects of the small-scale roughness on lunar TBs are just our study goal.

[8] *Ulaby et al*. [1987] modeled the effects of varying large-scale (tens to hundreds of wavelengths) roughness on the emissivity. It is shown that the emission begins to increase only when the RMS slope is 20° or bigger. The large-scale roughness of the maria is much smaller than 20° [*Golden*, 1979]. So for the maria, the large-scale roughness can be ignored, and only the small-scale roughness needs to be considered. Based on 2.38 GHz microwave radiometer measurements for Venus from Magellan data sets, *Campbell* [1994] found that the emissivity can be modeled by the behavior of a single dielectric surface with variable small-scale roughness, which can produce "diffuse" contribution. Especially for the multichannel radiometers on CE-1, where the incidence angle is 0°, the small-scale roughness would have significant effects on TBs, as is known from the results of emitting from two-scale rough sea surfaces [*Jin*, 1998].

[9] In the paper, the small perturbation method (SPM) is utilized to study the effect of the small-scale roughness of the lunar surface on TBs, since the SPM is valid when the standard deviation of the rough lunar surface is much smaller than the wavelength. To increase the accuracy of the emission, the second-order SPM transmittances are used because the second-order solution is necessary to ensure energy conservation [*Chen et al*., 2011]. Meanwhile, the noncoherent method is utilized to calculate the emission of the nonuniform regolith which can be discretized to a multilayer planar layered media. Therefore, based on the second-order SPM and the radiative transfer theory, a new model is developed for thermal microwave emission from the stratified media with a slightly rough top surface. Then, the presented model is utilized to simulate the microwave TBs at the Apollo 12 area, which is a typical mare area, under different small-scale roughness, incidence angle, and frequency. The simulation results show that a small-scale roughness will increase or decrease the microwave TBs of the lunar surface, and the change is related to the small-scale roughness, incidence angle, frequency, and polarization. For the CE-1 radiometer, where the incidence angle is 0°, the small-scale roughness will increase the TBs.

2. Formulation of the TB Model for the Lunar Regolith

[10] The lunar surface layer can be divided into the regolith layer and the underlying rock media [*Ouyang*, 2005]. However, there are no clear interfaces between the layers. For passive microwave remote sensing of lunar, the underlying rock media is usually regarded as a homogeneous isothermal medium, while the regolith layer is usually regarded as the soil with nonuniform temperature T and permittivity ε profiles. ε can be defined as [*Keihm and Langsth*, 1973]

$$\begin{cases} \varepsilon' = 1.919^{\rho} \\ \varepsilon'' = \varepsilon' \cdot 10^{0.038S + 0.312\rho - 3.260} \end{cases} \tag{1}$$

where ε' and ε'' are the real and imaginary parts of complex permittivity, respectively. S (%) is the $FeO + TiO_2$ abundance, and $\rho(g/cm^3)$ is the lunar regolith bulk density depending on depth [*Keihm and Langsth*, 1973], i.e.,

$$\rho = 1.92\frac{z + 12.2}{z + 18} \tag{2}$$

where z (in centimeters) is the lunar regolith depth.

2.1. Lunar Surface Layer Structure Model

[11] A lunar surface layer structure can be divided into the regolith layer and the underlying rock media, as shown in Figure 1. Furthermore, to consider the nonuniform permittivity ε profiles of the regolith, usually, the regolith layer is subdivided into multilayers. The change of permittivity at interfaces between adjacent layers in the regolith is so small that the effects of the roughness of interfaces on the radiation can be neglected, that is, the interfaces between the regolith sublayers are considered as planes. However, the top surface of the regolith layer is the interface between the vacuum and the regolith,

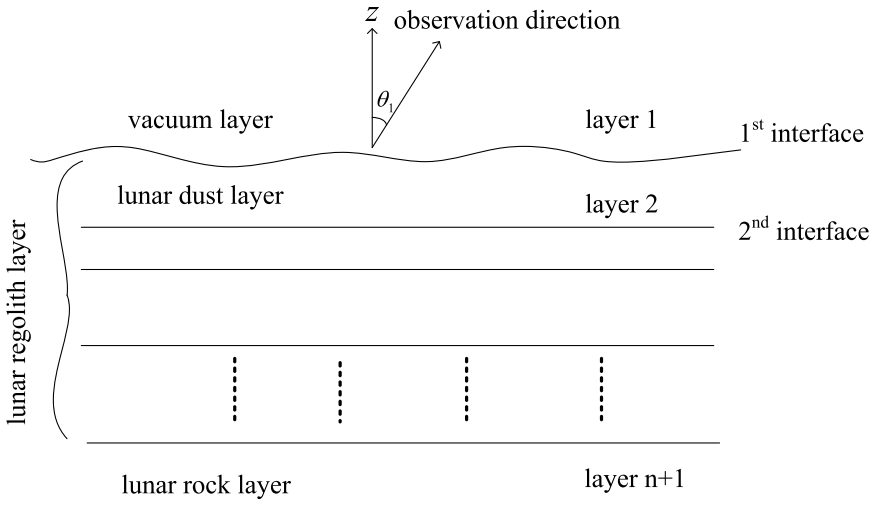

Figure 1. Stratified model of the lunar surface.

where the permittivity suddenly changes, so it should be seen as a slightly rough surface at the microwave frequency we are interested in. The vacuum is considered as the first layer and the underlying rock media as the $(n+1)$th layer. The ith layer is bounded on the top by the $(i-1)$th surface and on the bottom by the ith surface. The first interface is the rough surface with mean plane z = 0. The ith layer is characterized by a complex permittivity $\varepsilon_i = \varepsilon_{R,i} - j\varepsilon_{I,i}$, the complex wave impedance η_i, an absorption coefficient κ_{ei}, and a complex wave number $k_i = \omega\sqrt{\mu_0\varepsilon_i}$, where μ_0 is the magnetic permeability and ω is the frequency in radians per second. In addition, if we write $k_i = \beta_i - j\alpha_i$, then β_i is the phase constant, and α_i is the attenuation constant. The complex permittivity is almost constant across the dust layer with a depth of 2 cm [*Zheng*, 2005], which is set as the top layer of the regolith, that is, the second layer shown in Figure 1

2.2. Temperature Profile

[12] To calculate the lunar TBs, we need to know the temperature profile in advance, which can be obtained by solving the following heat conduction equation:

$$\frac{\partial}{\partial z}\left[K(z,T)\frac{\partial T}{\partial z}\right] + Q(z,T) = \rho(z,T)c(z,T)\frac{\partial T}{\partial z} \qquad (3)$$

where $\rho(z,T)$, $c(z,T)$, and $K(z,T)$ are the bulk density, specific heat, and heat conductivity at temperature T and depth z, respectively. $Q(z,T)$ is the constant flux originating from internal heat sources, which is negligible.

[13] Here the regolith is divided into two layers that differ in thermal conductivity [*Mitchell and de Pater*, 1994; *Vasavada et al*., 1999]. The thermal conductivity has the form $K = K_c\left[1 + \chi\left(\frac{T}{T_{350}}\right)^3\right]$, where T is temperature, K_c is the solid conductivity, and χ is the ratio of radiative to solid conductivity at a temperature of 350 K. For the top layer which extends from the surface to a depth of 2 cm, we have $K_c = 9.22 \times 10^{-4}$ W m^{-1} K^{-1} and $\chi = 1.48$ [*Li et al*., 2009]. For the following layer, which ranges from 2 cm to the depth of the regolith, we have $K_c = 4 \times 10^{-2}$ W m^{-1} K^{-1}, and $\chi = 1.48$ according to the data from *Vasavada et al*. [1999]. The heat capacity has the form $C(T) = c_1T^3 + c_2T^2 + c_3T + c_4$ [*Vasavada et al*., 1999], with $c_1 = 0.03142 \cdot 10^{-7}$, $c_2 = -0.03366 \cdot 10^{-4}$, $c_3 = 0.15899 \cdot 10^{-2}$,and $c_4 = -0.05277$.

[14] Figure 2 shows the simulated surface temperature as a function of local time at Apollo 15, which is compared with the measured surface temperature at Apollo 15. The horizontal axis is the hours after noon. Obviously, the simulation result is well coincident with the measured data [*Wieczorek and Huang*, 2006].

2.3. Equivalent TB Model

[15] Since all interfaces but the top are plane, we can derive out the TB contributions from the $n-1$ layers below the dust layer by the model [*Burke et al*., 1979] for the stratified medium with plane interfaces. Then, the contribution from the $n-1$ layers can be seen as the one from an equivalent layer, which is named the third layer. As shown in Figure 3, the vacuum is the first layer, the dust layer is the second layer, and the equivalent is the third layer.

[16] The TB $T_{B,p}(\theta_1,\phi_1,1^+)$ viewed from the vacuum at a nadir angle θ_1 (also called incidence angle) and an azimuth

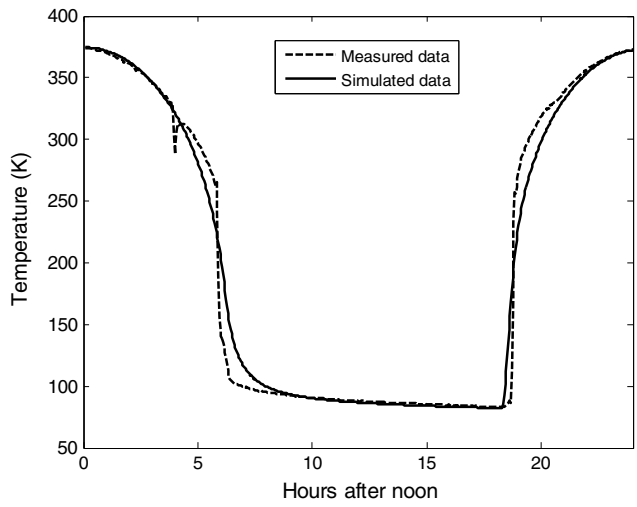

Figure 2. Comparison of the simulation and measurement of surface temperatures during a lunation at Apollo 15.

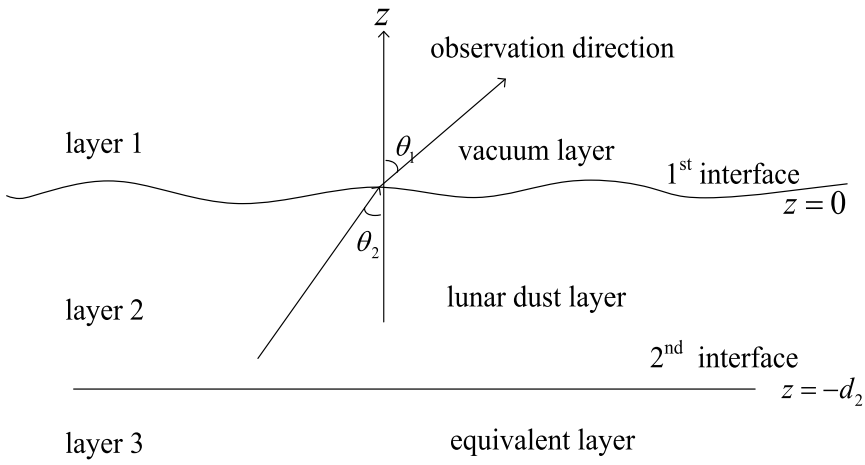

Figure 3. Equivalent stratified model of the lunar surface.

angle ϕ_1 are composed of two parts: (1) $T_{B2,p}(\theta_1,\phi_1,1^+)$, the contribution from the radiation of the second layer; and (2) $T_{B3,p}(\theta_1,\phi_1,1^+)$, the contribution from the radiation of the third layer, where 1^+ corresponds to a point located just above the first interface. Then, the total observed TB in p polarization is $T_{B,p}(\theta_1,\phi_1,1^+)=T_{B3,p}(\theta_1,\phi_1,1^+)+T_{B2,p}(\theta_1,\phi_1,1^+)$, where p can be h, the horizontal polarization, or v, the vertical polarization. For simplicity, all contributions involving second- or higher-order reflections will be ignored when calculating $T_{B,p}(\theta_1,\phi_1,1^+)$. Then, $T_{B2,p}(\theta_1,\phi_1,1^+)$ includes both the upward radiation of layer 2 $T_{B2\_up,p}(\theta_1,\phi_1,1^+)$ and the downward radiation of layer 2 reflected at the second interface and attenuated by this layer $T_{B2\_dn,p}(\theta_1,\phi_1,1^+)$. $T_{B3,p}(\theta_1,\phi_1,1^+)$ only includes the upward radiation of layer 3 attenuated by layer 2.

2.3.1. $T_{B3,p}(\theta_1,\phi_1,1^+)$

[17] It is assumed that the TB in the direction of θ_2 just above the second interface from the radiation of layer 3 is $T_{B3,p}(\theta_2,2^+)$, which then transmits to the direction of observation (θ_1,ϕ_1) in layer 1. We have

$$T_{B3,p}(\theta_1,\phi_1,\theta_2,\phi_2,1^+)=\frac{T_{B3,p}(\theta_2,2^+)}{L_2}\cdot t_{pp}^{12}(\theta_1,\phi_1,\theta_2,\phi_2)\cdot\frac{\varepsilon_2}{\varepsilon_1}+\frac{T_{B3,q}(\theta_2,2^+)}{L_2}\cdot t_{pq}^{12}(\theta_1,\phi_1,\theta_2,\phi_2)\cdot\frac{\varepsilon_2}{\varepsilon_1} \tag{4}$$

where $L_2=e^{\kappa_{e2}\cdot d_2\sec\theta_2}$ and $\kappa_{e2}\approx \mathrm{Im}\left(2\omega\sqrt{\mu_0\varepsilon_2}\right)$ if ignoring the effect of volume scattering. $t_{pq}^{12}(\theta_1,\phi_1,\theta_2,\phi_2)$ is the bidirectional transmission coefficient for q polarization incident of layer 2 in the direction (θ_2,ϕ_2) and the p polarization transmitted wave of layer 1 in the direction (θ_1,ϕ_1), where p can be h or v. Since the distribution of local elevations for lunar soil is typically well described by Gaussian statistics [*Helfenstein and Shepard*, 1999], then the lunar surface of small-scale roughness is assumed Gaussian here, i.e., the Gaussian height distribution and Gaussian autocorrelation function $W(\cdot)$, as used in Appendix. We utilize the second-order SPM to calculate the bidirectional transmission coefficient [*Chen et al*., 2011] $t_{pq}^{12}(\theta_1,\phi_1,\theta_2,\phi_2)$. It can be divided into zero-order contribution $t_p^{(0)}(\theta_{2c},\phi_{2c})$, first-order contribution $t_{pp}^{(1)12}(\theta_1,\phi_1,\theta_2,\phi_2)$ and $t_{pq}^{(1)12}(\theta_1,\phi_1,\theta_2,\phi_2)$, and second-order contribution $t_p^{(2)}(\theta_{2c},\phi_{2c})$, where θ_{2c},ϕ_{2c} correspond to the direction of coherent transmission, determined by $k_1\sin\theta_1=k_2\sin\theta_{2c}$, $\phi_{2c}=\phi_1$. Then, we have

$$\begin{aligned}T_{B3,p}(\theta_1,\phi_1 1^+)=&\int_0^{2\pi}d\phi_2\int_0^{\pi/2}\sin\theta_2 d\theta_2[T_{B3,p}(\theta_2,\phi_2,2^+)\\&\cdot\frac{1}{L_2}\cdot t_{pp}^{(1)12}(\theta_1,\phi_1,\theta_2,\phi_2)\cdot\frac{\varepsilon_2}{\varepsilon_1}\\&+\int_0^{2\pi}d\phi_2\int_0^{\pi/2}\sin\theta_2 d\theta_2[T_{B3,q}(\theta_2,\phi_2,2^+)\\&\cdot\frac{1}{L_2}\cdot t_{pq}^{(1)12}(\theta_1,\phi_1,\theta_2,\phi_2)]\cdot\frac{\varepsilon_2}{\varepsilon_1}\\&+T_{B3,p}(\theta_{2c},\phi_{2c},2^+)\cdot\frac{1}{L_2}\cdot t_p^{(0)}(\theta_{2c},\phi_{2c})\\&+T_{B3,p}(\theta_{2c},\phi_{2c},2^+)\cdot\frac{1}{L_2}\cdot t_p^{(2)}(\theta_{2c},\phi_{2c}).\end{aligned} \tag{5}$$

[18] The expressions of $t_p^{(0)}(\theta_{2c},\phi_{2c})$, $t_p^{(2)}(\theta_{2c},\phi_{2c})$, $t_{pp}^{(1)12}(\theta_1,\phi_1,\theta_2,\phi_2)$, and $t_{pq}^{(1)12}(\theta_1,\phi_1,\theta_2,\phi_2)$ are given in the Appendix, and the derivation is given by *Chen et al*. [2011].

[19] In (5), the first and second terms on the right side are the contribution of the first-order transmission, corresponding to the no-coherent transmission, while the third and fourth terms are the contributions of the zero- and second-order coherent transmissions.

[20] Using the method by *Burke et al*. [1979], we can obtain the TB just above the second interface from the radiation of layer 3, $T_{B3,p}(\theta_2,2^+)$, which is the contribution of the upward radiation of the rock media and all the regolith but the dust layer, i.e.,

$$T_{B3,p}(\theta_2,2^+)=\left(1-\Gamma_{2,p}(\theta_2)\right)\sum_{i=3}^{N+1}\left\{T_{s,i}\left(1-\frac{1}{L_i}\right)\left(1+\frac{\Gamma_{i,p}(\theta_i)}{L_i}\right)\prod_{j=4}^{i}\left[\frac{1-\Gamma_{j-1,p}(\theta_{j-1})}{L_{j-1}}\right]\right\} \tag{6}$$

where $T_{s,i}$ is the physical temperatures of the ith layer; $L_i=\exp(\kappa_{ei}\cdot d_i\cdot\sec\theta_i)$, $\kappa_{ei}\approx\mathrm{Im}\left(2\omega\sqrt{\mu_0\varepsilon_i}\right)$, d_i is the thickness of the ith layer, the refraction angle in the ith layer defined relative to the zenith is θ_i, which is related to θ_{i+1} by Snell's

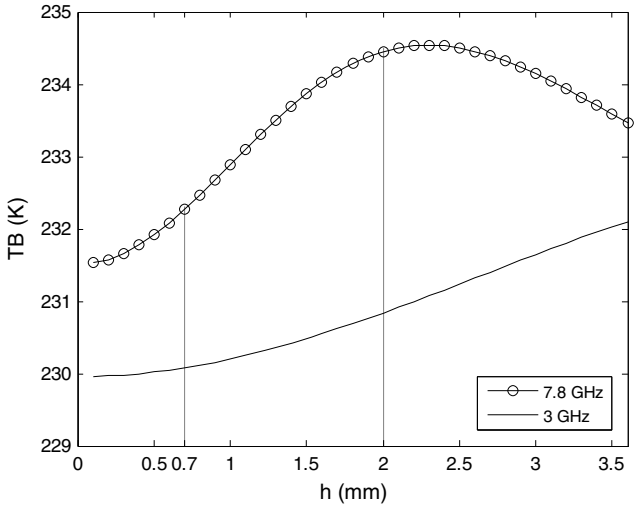

Figure 4. TBs at the Apollo12 area as a function of h when the incidence angle is 0°, $m = 0.29$.

law $\sin\theta_i = \frac{k_{i+1}}{k_i}\sin\theta_{i+1}$, $\Gamma_{i,p}(\theta_i) = |R_{i,p}(\theta_i)|^2$, and the Fresnel coefficients $R_{i,p}(\theta_i)$ for the horizontal and vertical polarizations, respectively, are

$$R_{i,h} = \frac{\eta_{i+1}\cos\theta_{i-1} - \eta_i\cos\theta_i}{\eta_{i+1}\cos\theta_{i-1} + \eta_i\cos\theta_i}, R_{i,v} = \frac{\eta_i\cos\theta_{i-1} - \eta_{i+1}\cos\theta_i}{\eta_i\cos\theta_{i-1} + \eta_{i+1}\cos\theta_i},$$
$$\eta_i = \sqrt{\frac{\mu_0}{\varepsilon_i}}.$$

[21] Because layer 3 is semi-infinite, its effective reflectivity is defined as $r_{3,p}(\theta_2, 2^+) = 1 - \frac{T_{B3,p}(\theta_2,2^+)}{T_g}$. If it is assumed that $T_{s,i} = T_g$, then $r_{3,p}(\theta_2,2^+)$ can be written as

$$r_{3,p}(\theta_2, 2^+) = 1 - \left(1 - \Gamma_{2,p}(\theta_2)\right)\sum_{i=3}^{N+1} \left\{\left(1 - \frac{1}{L_i}\right)\left(1 + \frac{\Gamma_{i,p}(\theta_i)}{L_i}\right)\prod_{j=4}^{i}\left[\frac{1 - \Gamma_{j-1,p}(\theta_{j-1})}{L_{j-1}}\right]\right\}. \quad (7)$$

2.3.2. $T_{B2,p}(\theta_1,\phi_1,1^+)$

[22] As is shown above, $T_{B2,p}(\theta_1,\phi_1,1^+)$ includes both the layer 2's upward radiation, $T_{B2\_up,p}(\theta_1,\phi_1,1^+)$, and the layer 2's downward radiation reflected at the second interface and attenuated by this layer, $T_{B2\_dn,p}(\theta_1,\phi_1,1^+)$.

2.3.2.1. $T_{B2\_up,p}(\theta_1,\phi_1,1^+)$

[23] We can write $T_{B2\_up,p}(\theta_1,\phi_1,1^+)$ as

$$\begin{aligned} T_{B2_{\mathrm{up}},p}(\theta_1,\phi_1 1^+) = {} & \int_0^{2\pi} d\phi_2 \int_0^{\pi/2} \sin\theta_2 d\theta_2 \cdot T_{B2_{\mathrm{up}},p}(\theta_2,\phi_2,1^-)\cdot \\ & t_{pp}^{(1)12}(\theta_1,\phi_1,\theta_2,\phi_2)\cdot\frac{\varepsilon_2}{\varepsilon_1} \\ & + \int_0^{2\pi} d\phi_2 \int_0^{\pi/2} \sin\theta_2 d\theta_2 \cdot T_{B2_{\mathrm{up}},q}(\theta_2,\phi_2,1^-)\cdot \\ & t_{pq}^{(1)12}(\theta_1,\phi_1,\theta_2,\phi_2)\cdot\frac{\varepsilon_2}{\varepsilon_1} \\ & + T_{B2_{\mathrm{up}},p}(\theta_{2c},\phi_{2c},1^-)\cdot t_p^{(0)}(\theta_{2c},\phi_{2c}) \\ & + T_{B2_{\mathrm{up}},p}(\theta_{2c},\phi_{2c},1^-)\cdot t_p^{(2)}(\theta_{2c},\phi_{2c}) \end{aligned} \quad (8)$$

where $T_{B2\_up,p}(\theta_2,\phi_2,1^-)$ and $T_{B2\_up,q}(\theta_2,\phi_2,1^-)$ are the TBs just below the first interface from the upward radiation of layer 2 in p and q polarizations, respectively. Since layer 2 is approximately uniform and its temperature varies with depth, we can derive out $T_{B2\_up,p}(\theta_2,1^-)$ and $T_{B2\_up,q}(\theta_2,1^-)$ by using the radiation transfer theory

$$\begin{aligned} T_{B2_{\mathrm{up}},p}(\theta_2,1^-) = T_{B2_{\mathrm{up}},q}(\theta_2,1^-) = {} & T_0\left(1 - \frac{1}{L_2}\right) \\ & + g\left[\frac{d_2}{L_2} - \frac{1}{k_{e2}\sec\theta_2}\left(1 - \frac{1}{L_2}\right)\right] \end{aligned} \quad (9)$$

where T_0 is the surface temperature, and g is the temperature varying rate in the dust layer.In (8), the first and second terms are the contributions of the noncoherent radiation, and the third and fourth terms are the coherent contributions.

2.3.2.2. $T_{B2\_dn,p}(\theta_1,\phi_1,1^+)$

[24] It is assumed that $T_{B2\_dn,p}(\theta_2,2^+)$ and $T_{B2\_dn,q}(\theta_2,2^+)$ are the TBs just above the second interface from the downward going radiation of layer 2 in p and q polarizations, respectively. Then, we can write $T_{B2\_dn,p}(\theta_1,\phi_1,1^+)$ as

$$\begin{aligned} T_{B2_{\mathrm{dn}},p}(\theta_1,\phi_1 1^+) = {} & \int_0^{2\pi} d\phi_2 \int_0^{\pi/2} \sin\theta_2 d\theta_2 \cdot T_{B2_{\mathrm{dn}},p}(\theta_2,\phi_2,2^+)\cdot \\ & r_{3,p}(\theta_2,2^+)\cdot\frac{1}{L_2}\cdot t_{pp}^{(1)12}(\theta_1,\phi_1,\theta_2,\phi_2)\cdot\frac{\varepsilon_2}{\varepsilon_1} \\ & + \int_0^{2\pi} d\phi_2 \int_0^{\pi/2} \sin\theta_2 d\theta_2 \cdot T_{B2_{\mathrm{dn}},q}(\theta_2,\phi_2,2^+)\cdot \\ & r_{3,q}(\theta_2,2^+)\cdot\frac{1}{L_2}\cdot t_{pq}^{(1)12}(\theta_1,\phi_1,\theta_2,\phi_2)\cdot\frac{\varepsilon_2}{\varepsilon_1} \\ & + T_{B2_{\mathrm{up}},p}(\theta_{2c},\phi_{2c},2^+)\cdot r_{3,p}(\theta_{2c},2^+) \\ & \cdot\frac{1}{L_2}\cdot t_p^{(0)}(\theta_{2c},\phi_{2c}) + T_{B2_{\mathrm{up}},p}(\theta_{2c},\phi_{2c},2^+)\cdot \\ & r_{3,p}(\theta_{2c},2^+)\cdot\frac{1}{L_2}\cdot t_p^{(2)}(\theta_{2c},\phi_{2c}) \end{aligned} \quad (10)$$

where $T_{B2_{\mathrm{dn}},p}(\theta_2,2^+) = T_{B2_{\mathrm{dn}},q}(\theta_2,2^+) = T_0\left(1 - \frac{1}{L_2}\right) + g\left[-d_2 + \frac{1}{k_{e2}\sec\theta_2}\left(1 - \frac{1}{L_2}\right)\right]$.

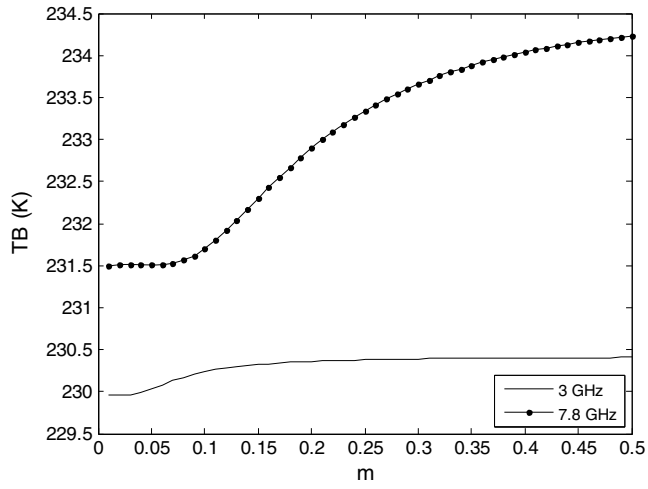

Figure 5. TBs at the Apollo12 area as a function of m when the incidence angle is 0°, $h = 1.35$ mm.

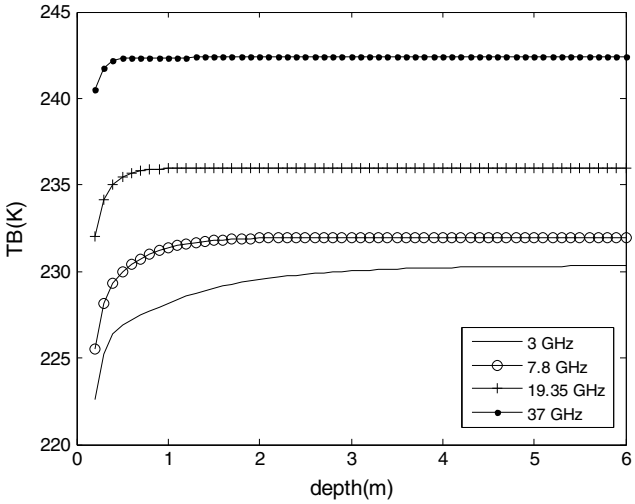

Figure 6. TBs varying with regolith depth when the incidence angle is 0°, $S = 18.38$.

[25] Finally, the total TB viewed in the direction (θ_1,ϕ_1) by the radiometer is $T_{B,p}(\theta_1,\phi_1,1^+) = T_{B3,p}(\theta_1,\phi_1,1^+) + T_{B2\_up,p}(\theta_1,\phi_1,1^+) + T_{B2\_dn,p}(\theta_1,\phi_1,1^+)$.

3. Simulations and Discussions

[26] According to the model above, the TBs of the typical mare area, i.e., the Apollo 12 area, are simulated under different small-scale roughness values. For simplicity, the mare surface is assumed to be isotropic Gaussian, then the TBs are irrelevant to the azimuth angle ϕ_1 of the radiometer. The effects of small-scale roughness, incidence angle, frequency, and polarization on the TBs are analyzed.

[27] We first analyze the effects of RMS height deviation h and RMS slope m on the TBs at 3 and 7.8 GHz when the incidence angle is 0°. $m = \sqrt{2}h/l$, where l is the correlation length. According to the analysis of the sample of lunar maria [*Helfenstein and Shepard*, 1999], the average RMS slope angle is 16° for lunar maria, and h is in the range of 0.9–3.6 mm. Then, given $m = tg16° = 0.29$, the TBs at the Apollo 12 area varying with h are shown in Figure 4. It is shown that the TBs at the two frequencies increase with h. It is noted that the TB at 7.8 GHz decreases when h is about 2.3 mm, for this calculation of 7.8 GHz is already out of the validity of the second-order SPM for $h > 2$ mm [*Thorsos and Jackson*, 1989; *Li et al.*, 1999; *Sanchez-Gil et al.* 1995]. We can find that the TBs of 3 GHz increase by about 2 K when h increases from 0.9 to 3.6 mm. For the Apollo 12 area, the average range of elevations of h is 1.35 ± 0.64 mm, as shown in 0.7–2 mm, then the TB change of 3 GHz is about 0.5 K, and the TB change of 7.8 GHz is about 2 K.

Table 1. Three Surface-Roughness Conditions

Surface	h (mm)	l (mm)	m
S1	0.90	4.39	0.29
S2	1.80	7.27	0.35
S3	2.30	7.74	0.42

[28] Given $h = 1.35$ mm, the TBs at the Apollo 12 area varying with m are shown in Figure 5. It is shown that TBs at the two frequencies increase with m.

[29] Since a major goal of the CE'1 radiometer is to infer regolith properties and thickness, then we need to compare the range of expected temperatures due to regolith thickness with the likely range of roughness-induced changes. For the Apollo 12 area, the TBs varying with the regolith depth at the 0° incidence angle are shown in Figure 6, where the $FeO + TiO_2$ abundance $S = 18.38$. It is shown that the depths approaching the constant TBs at 37, 19.35, 7.8, and 3 GHz are about 0.5, 1, 2.2, and 4 m, respectively. From Figure 6, it is shown that only the 3 GHz channel has any chance of determining regolith thickness and only when the thickness is 4 m or less when $S = 18.38$. At greater thickness, there is no additional discrimination. It is noted that the $FeO + TiO_2$ abundance has a significant effect on the saturation depth, because it is directly related to the complex permittivity. Generally, the $FeO + TiO_2$ abundance in lunar maria is bigger than that in lunar highlands. For examples, in lunar maria, $S = 23.2$ at Apollo 11 and $S = 18.38$ at Apollo 12; in lunar highlands, $S = 12.12$ at Apollo 14 and $S = 5.55$ at Apollo 16. Figure 7 is same as Figure 6 but for $S = 5.55$. It

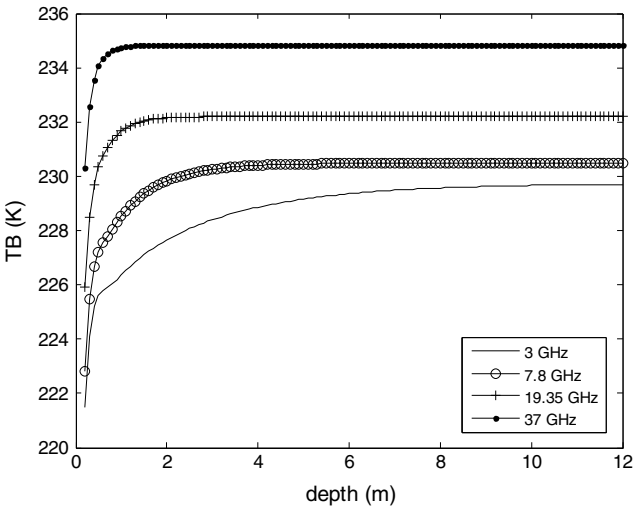

Figure 7. TBs varying with regolith depth when the incidence angle is 0°, $S = 5.5$.

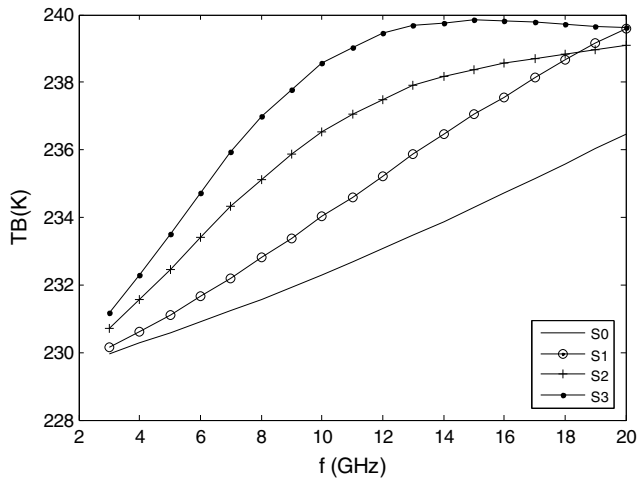

Figure 8. TBs varying with frequency when the incidence angle is 0°, under different small-scale roughness conditions.

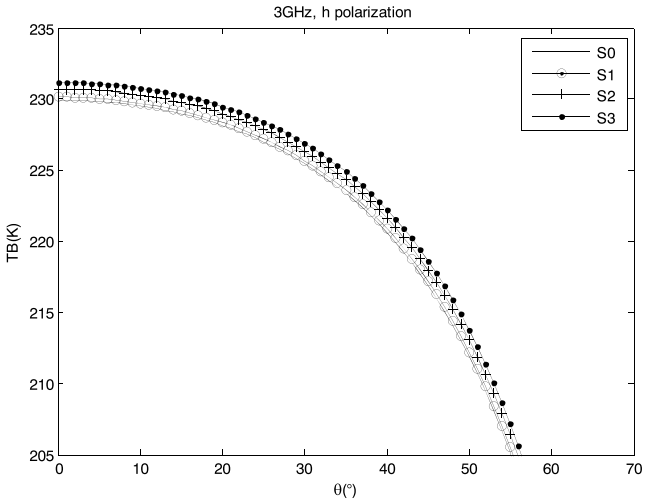

Figure 9. TBs varying with incidence angle at 3 GHz, *h* polarization.

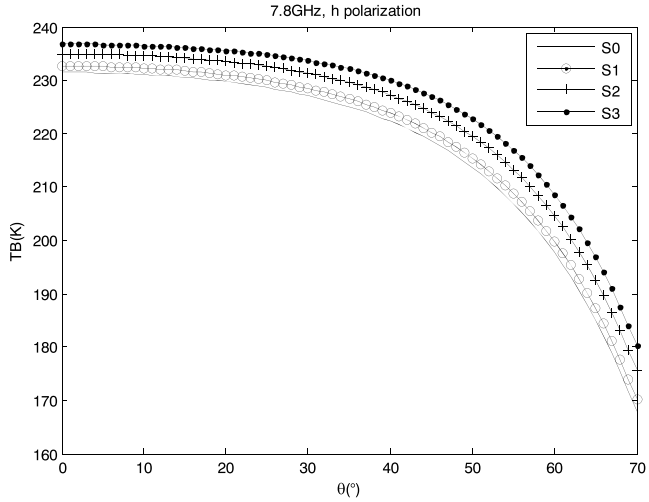

Figure 11. TBs varying with incidence angle at 7.8 GHz, *h* polarization.

shown that the saturation depths increase at all four frequencies, and the detectable thickness of 3 GHz is about 8 m. The detailed study on the $FeO + TiO_2$ abundance distribution of the whole Moon is available in *Yan et al*. [2012].

[30] Based on the analysis of the sample from Apollo12 [*Helfenstein and Shepard*, 1999], three surface-roughness conditions S1, S2, and S3 are chosen, as shown in Table 1, with *h* varying from about 0.9 to 2.3 mm, and RMS slope *m*, from about 0.29 to 0.42, *l* is the correlation length. In addition, S0 is referred to flat surface. Figure 8 gives TBs varying with frequency under these three surface-roughness conditions when incidence angle is 0°.

[31] From Figure 8, it is found that TB increases with increasing frequency for a flat surface S0 and small roughness surfaces S1 and S2. However, for a larger roughness surface S3, TB will decrease when frequency *f* is over about 15 GHz. This is because the calculation for $f > 10$ GHz for roughness S3 is out of the validity range of the second SPM [*Thorsos and Jackson*, 1989; *Li et al*., 1999; *Sanchez-Gil et al*., 1995]. So only the TBs at 3 and 7.8 GHz channels are simulated here.

[32] Figures 9–12 show that TB varies with incidence angle under *h* and *v* polarizations for 3 and 7.8 GHz, respectively.

[33] From Figure 9, TBs of rough surfaces for the horizontal polarization at 3 GHz are 1–2 K larger than that of the flat surface for all incidence angles. Larger roughness causes higher TB. From Figure 10, TBs of rough surfaces for the vertical polarization are 1–2 K larger when the incidence angle is 0°. The TB differences between rough and flat surfaces become smaller as the incidence angle increases.

[34] From Figure 11, for 7.8 GHz, TBs of rough surfaces for the horizontal polarization are 1–6 K larger than that of the flat surface for all incidence angles. As the same from Figure 9, larger roughness causes higher TB. From Figure 12, TBs of rough surfaces for the vertical polarization are 1–5 K larger when the incidence angle is 0°. For a larger incidence angle, the difference becomes smaller. When the incidence angle is larger than 40°, TBs of rough surfaces are lower than that of the flat surface.

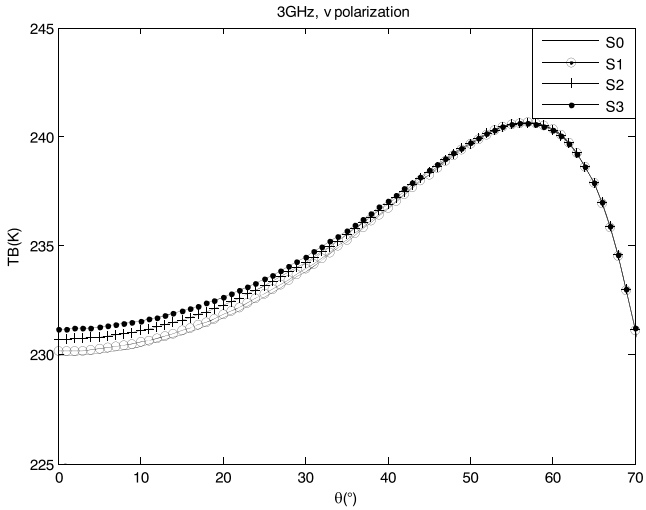

Figure 10. TBs varying with incidence angle at 3 GHz, *v* polarization.

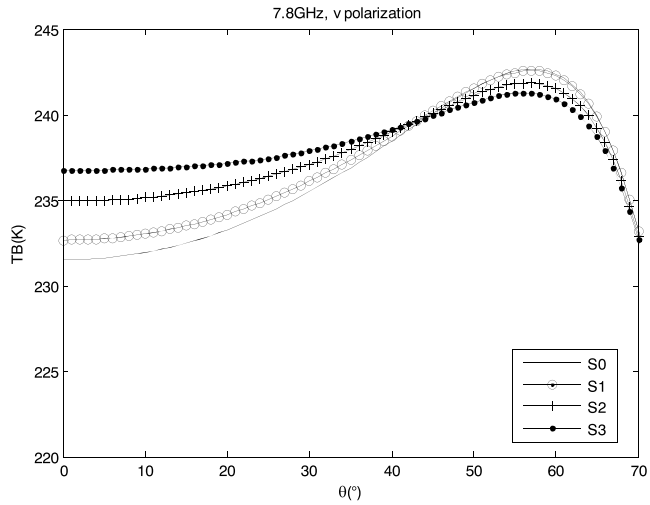

Figure 12. TBs varying with incidence angle at 7.8 GHz, *v* polarization.

4. Conclusions

[35] To study the effects of slight roughness of the lunar surface on TBs, we propose a microwave TB model by combining the radiative transfer theory and the second-order SPM. According to the model, the TBs of the typical mare area, i.e., the Apollo 12 area, under different roughness conditions are calculated. It is shown that:

1. When the incidence angle is 0°, a slightly rough surface will increase the microwave radiative TB of the lunar surface, and the increment is related to the frequency and the surface small-scale roughness parameters.

2. Under *h* polarization, the slightly rough surface will increase the microwave radiative TBs of lunar surfaces, and the TBs decrease when the incidence angle is rising, which is similar to the results given by *Shin and Kong* [1982].

3. Under *v* polarization, the small-scale roughness will increase the microwave radiative TBs of the lunar surface with small incidence angles, while the small-scale roughness will reduce the TBs with large incidence angles, which is also similar to the results given by *Shin and Kong* [1982].

4. Only the 3 GHz channel has any chance of determining regolith thickness, and the detectable thickness is closely related to the FeO + TiO2 abundance *S*. When $S = 18.38$, the detectable thickness is below about 4 m, while when $S = 5.5$, the detectable depth is about 8 m.

The uncertainties of 3 GHz TB linked with mean small-scale surface roughness at Apollo 12 are on the order of 0.5 K. In this area, the TB variation by the thickness from 1 to 4 m is about 2 K, and the effect of small-scale surface roughness should be considered in thickness inversion.

[36] The model we have proposed is applicable to flat terrains where the mean surface of the regolith surface can be considered as a plane, such as the maria. While for those areas with a greatly undulating terrain, the mean surface of which is no longer a plane, this model is no longer valid. In this case, the large-scale roughness needs to be considered further in the TB models.

[37] Although in the presented TB model a Gaussian height distribution and a Gaussian autocorrelation function are assumed for the mare surface of small roughness, the TB model can be also suitable for other kinds of small-scale rough surface, such as the unisotropic exponential autocorrelation surface and the fractal surface. The effects of different choices on TBs are worthy of further study.

Appendix

[38] Equation (5) is written again for convenience, i.e.,

$$
\begin{aligned}
T_{B3,p}(\theta_1,\phi_1,1^+) = & \int_0^{2\pi} d\phi_2 \int_0^{\pi/2} \sin\theta_2 d\theta_2 \\
& [T_{B3,p}(\theta_2,\phi_2,2^+)\cdot\frac{1}{L_2}\cdot t_{pp}^{(1)12}(\theta_1,\phi_1,\theta_2,\phi_2)\cdot\frac{\varepsilon_2}{\varepsilon_1} \\
& + \int_0^{2\pi} d\phi_2 \int_0^{\pi/2} \sin\theta_2 d\theta_2 [T_{B3,q}(\theta_2,\phi_2,2^+)\cdot\frac{1}{L_2}\cdot t_{pq}^{(1)12} \\
& (\theta_1,\phi_1,\theta_2,\phi_2)]\cdot\frac{\varepsilon_2}{\varepsilon_1} + T_{B3,p}(\theta_{2c},\phi_{2c},2^+)\cdot\frac{1}{L_2}\cdot t_p^{(0)}(\theta_{2c},\phi_{2c}) \\
& + T_{B3,p}(\theta_{2c},\phi_{2c},2^+)\cdot\frac{1}{L_2}\cdot t_p^{(2)}(\theta_{2c},\phi_{2c})
\end{aligned}
$$

where θ_{2c} corresponds to the direction of coherent transmission, which is determined by

$$k_1\sin\theta_1 = k_2\sin\theta_{2c},\ \phi_{2c} = \phi_1$$

$$t_{hh}^{(1)12}(\theta_1,\phi_1,\theta_2,\phi_2) = \frac{\eta_2}{\eta_1}k_1^2\cos\theta_1 W(\bar{k}_{1\perp}-\bar{k}_{2\perp})\left|f_{hh}^{(1)}(\bar{k}_{1\perp},\bar{k}_{2\perp})\right|^2$$

$$t_{vv}^{(1)12}(\theta_1,\phi_1,\theta_2,\phi_2) = \frac{\eta_2}{\eta_1}k_1^2\cos\theta_1 W(\bar{k}_{1\perp}-\bar{k}_{2\perp})\left|f_{vv}^{(1)}(\bar{k}_{1\perp},\bar{k}_{2\perp})\right|^2$$

$$t_{vh}^{(1)12}(\theta_1,\phi_1,\theta_2,\phi_2) = \frac{\eta_2}{\eta_1}k_1^2\cos\theta_1 W(\bar{k}_{1\perp}-\bar{k}_{2\perp})\left|f_{vh}^{(1)}(\bar{k}_{1\perp},\bar{k}_{2\perp})\right|^2$$

$$t_{hv}^{(1)12}(\theta_1,\phi_1,\theta_2,\phi_2) = \frac{\eta_2}{\eta_1}k_1^2\cos\theta_1 W(\bar{k}_{1\perp}-\bar{k}_{2\perp})\left|f_{hv}^{(1)}(\bar{k}_{1\perp},,\bar{k}_{2\perp})\right|^2$$

$$t_h^{(0)}(\theta_{2c},\phi_{2c}) = \frac{\sqrt{\varepsilon_2}}{\sqrt{\varepsilon_1}}|1+R_{h0}(\theta_{2c})|^2\ t_v^{(0)}(\theta_{2c},\phi_{2c}) = \frac{\varepsilon_2\sqrt{\varepsilon_2}}{\varepsilon_1\sqrt{\varepsilon_1}}|1+R_{v0}(\theta_{2c})|^2$$

$$R_{h0} = \frac{k_2\cos\theta_{2c}-k_1\cos\theta_1}{k_2\cos\theta_{2c}+k_1\cos\theta_1}\ R_{v0} = \frac{k_1^2k_2\cos\theta_{2c}-k_2^2k_1\cos\theta_1}{k_1^2k_2\cos\theta_{2c}+k_2^2k_1\cos\theta_1}$$

where k_2, η_2, and ε_2 are the wave number, wave impedance, and permittivity of layer 2, respectively, and k_1, η_1, and ε_1 are the wave number, wave impedance, and permittivity of layer 1, respectively. Thus

$$
\begin{aligned}
t_h^{(2)}(\theta_{2c},\phi_{2c}) &= 2\mathrm{Re}\left[\frac{\sqrt{\varepsilon_2}}{\sqrt{\varepsilon_1}}\cdot(1+R_{h0})\cdot f_{\mathrm{hh}}^{*(2)}(k_{2\perp})\right], \quad t_v^{(2)}(\theta_{2c},\phi_{2c}) \\
&= 2\mathrm{Re}\left[\frac{\varepsilon_2}{\varepsilon_1}\cdot(1+R_{v0})\cdot f_{\mathrm{vv}}^{*(2)}(k_{2\perp})\right]
\end{aligned}
$$

$$
\begin{aligned}
f_{hh}^{(2)}(\bar{k}_{2\perp}) = & \frac{k_{zi}(k_1^2-k_2^2)}{(k_{zi}+k_{1zi})^2}\left\{(k_{1zi}-k_{zi})\int_{-\infty}^{\infty}d\bar{k}_{1\perp}W(\bar{k}_{1\perp}-\bar{k}_{2\perp})\right. \\
& -2(k_1^2-k_2^2)\int_{-\infty}^{\infty}d\bar{k}_{1\perp}W(\bar{k}_{1\perp}-\bar{k}_{2\perp}) \\
& \left.\cdot\left[\sin^2(\phi_1-\phi_2)\frac{k_zk_{1z}}{k_1^2k_z+k_2^2k_{1z}} + \cos^2(\phi_1-\phi_2)\frac{1}{k_{1z}+k_z}\right]\right\}
\end{aligned}
$$

$$
\begin{aligned}
f_{vv}^{(2)}(\bar{k}_{2\perp}) = & \frac{k_1(k_1^2-k_2^2)k_{zi}}{(k_1^2k_{zi}+k_2{}^2k_{1zi})^2}\left\{\int_{-\infty}^{\infty}d\bar{k}_{1\perp}W(\bar{k}_{1\perp}-\bar{k}_{2\perp})k_2(k_1^2k_{zi}-k_2^2k_{1zi}) + 2\int_{-\infty}^{\infty}d\bar{k}_{1\perp}W(\bar{k}_{1\perp}-\bar{k}_{2\perp})\right. \\
& \cdot\left[-k_2k_{zi}k_{1zi}\left(k_1^2-k_2^2,k_z+k_{1z}\sin^2(\phi_1-\phi_2)+\frac{1}{k_1^2k_z+k_2^2k_{1z}}-k_2(k_1^2-k_2{}^2)k_{\rho i}^2k_\rho^2\right)+k_\rho k_{\rho i}k_2(k_z+k_{1z})(k_2^2k_{1zi}-k_1^2k_{zi})\right. \\
& \left.\left.\cos(\phi_1-\phi_2)-k_2k_zk_{1z}k_{zi}k_{1zi}(k_1^2-k_2{}^2)\cos^2(\phi_1-\phi_2))\right]\right\}.
\end{aligned}
$$

[39] For the isotropic Gaussian correlation function

$$W(\bar{k}_{1\perp}-\bar{k}_{2\perp})=\frac{h^2l^2}{4\pi}\exp(-\frac{\left(k_\rho^2+k_{\rho i}^2\right)l^2}{4}+\frac{k_\rho k_{\rho i}l^2}{2}\cos(\phi_1-\phi_2))$$

$$k_{zi}=k_2\cos\theta_{2c},k_{1zi}=\sqrt{k_1^2-k_2^2\sin^2\theta_{2c}},k_{1z}=k_1\cos\theta_1,k_z=\sqrt{k_2^2-k_1^2\sin^2\theta_1},k_{\rho i}=k_2\sin\theta_{2c},k_\rho=k_1\sin\theta_1,$$

$$\bar{k}_{1\perp}=k_{1x}\hat{x}+k_{1y}\hat{y}=k_\rho\cos\phi_1\hat{x}+k_\rho\sin\phi_1\hat{y},\bar{k}_{2\perp}=k_{2x}\hat{x}+k_{2y}\hat{y}=k_{\rho i}\cos\phi_2\hat{x}+k_{\rho i}\sin\phi_2\hat{y}.$$

[40] **Acknowledgments.** This paper was supported by the National Science Foundation of China (40971185) and the National High Technology Research and Development Program (2010AA122200). The authors would like to thank the anonymous reviewers for the many insightful comments to improve the presentation.

References

Burke, W. J., T. Schmugge, and J. F. Paris (1979), Comparison of 2.8- and 21-cm microwave radiometer observations over soils with emission model calculations, *J. Geophys. Res.*, *84*(C1), 287–294, doi:10.1029/JC084iC01p00287.

Campbell, B. A. (1994), Merging Magellan emissivity and SAR data for analysis of Venus surface dielectric properties, *Icarus*, *112*(1), 187–203, doi:10.1006/icar.1994.1177.

Chen, P., Y. Tian, L. Hua, D. W. Song, Q. X. Li, Q. L. Huang, and L. Q. Gui (2011), Second-order small perturbation method for transmission from dielectric rough surfaces, *Waves Random Complex Media*, *21*(4), 668–689, doi:10.1080/17455030.2011.626809.

Fa, W., and Y. Q. Jin (2007a), Simulation of TB of lunar surface and inversion of the regolith layer thickness, *J. Geophys. Res.*, *112*, E05003, doi:10.1029/2006JE002751.

Fa, W., and Y. Q. Jin (2007b), Quantitative estimation of helium-3 spatial distribution in the lunar regolith layer, *Icarus*, *71*, 15–23, doi:10.1016/j.icarus.2007.03.014.

Fa, W., and Y. Q. Jin (2011), Analysis of microwave TB of lunar surface and inversion of regolith layer thickness: Primary results from Chang-E 1 multi-channel radiometer observation, *Sci. China Inf. Sci.*, *53*, 168–181, doi:10.1007/s11432-010-0020-1.

Golden, L. M. (1979), The effect of surface roughness on the transmission of microwave radiation through a planetary surface, *Icarus*, *38*(3), 451–455, doi:10.1016/0019-1035(79)90199-4.

Helfenstein, P., and M. K. Shepard (1999), Submillimeter-scale topography of the lunar regolith, *Icarus 141*, 107–131, doi:10.1006/icar.1999.6160.

Jin, Y. Q. (1998), *Remote Sensing Theory of Electromagnetic Scattering and Thermal Emission*, Science, China.

Jin, Y. Q., and W. Z. Fa (2011), The modeling analysis of microwave emission from stratified media of non-uniform lunar cratered terrain surface in Chinese Chang-E 1 observation, Chin. Sci. Bull., *56*(11), 1165–1171, doi:10.1007/s11434-011-4480-5.

Keihm, S. J. (1984), Interpretation of the lunar microwave TB spectrum: Feasibility of orbital heat flow mapping, *Icarus*, *60*(3), 568–589, doi:10.1016/0019-1035(84)90165-9.

Keihm, S. J., and M. G. Langsth (1973), Surface TBs at the Apollo 17 heat flow site: Thermal conductivity of the upper 15 cm of regolith, paper presented at Proc. 4th Lunar *Sci*. Conf., 2503–2513.

Li, Q., L. Tsang, K. Pak, and C. H. Chan (1999), Monte-Carlo simulations of emissivities of random dielectric rough surfaces and comparisons with the small perturbation method, paper presented *at* Proc. IEEE Int. Geosci. Remote Sens. Symp. *(IGARSS'99)*, *5*, 2422–2424, doi:10.1109/IGARSS.1999.771530.

Li, Y., Z. Z. Wang, and J. S. Jiang (2009), Influence of lunar surface temperature profiles on TB of CE-1 lunar microwave sounder (in Chinese), *Sci. China Ser. D*, *39*(8), 1045–1058.

Meng, Z. G., S. B. Chen, C. Liu, X. J. Du, and H. Liu (2008), Simulation on passive microwave radiative transfer in inhomogeneous lunar regolith (in Chinese), *J. Jilin Univ. (Earth Sci. Ed.)*, *38*(5), 1070–1074.

Mitchell, D. L., and I. de Pater (1994), Microwave imaging of Mercury's thermal emission at wavelengths from 0.3 to 20.5 cm, *Icarus*, *110*, 2–32.

Ouyang, Z. Y. (2005), *Introduction to Lunar Science (in Chinese)*, China Astronautic Publishing House, Beijing, China.

Sanchez-Gil, J. A., A. A. Maradudin, and E. R. Mendez (1995), Limits of validity of three perturbation theories of the specular scattering of light from one-dimensional, randomly rough, dielectric surfaces, *J. Opt. Soc. Am. A Opt. Image Sci*., *12*(7), 1547–1558, doi:10.1364/JOSAA.12.001547.

Shin, R. T., and J. A. Kong (1982), Theory for thermal microwave emission from a homogeneous layer rough surface containing spherical scatterers, *J. Geophys. Res.*, *87*(B7), 5566–5576, doi:10.1029/JB087iB07p05566.

Smith, B. G. (1967), Lunar surface roughness: Shadowing and thermal emission, *J. Geophys. Res.*, *72*(16), 4059–4067, doi:10.1029/JZ072i016p04059.

Thorsos, E. I., and D. R. Jackson (1989), The validity of the perturbation approximation for rough surface scattering using a Gaussian roughness spectrum, *J. Acoust. Soc. Am.*, *86*(1), 261–277, doi:10.1121/1.398342.

Tsang, L., P. Xu, and K. S. Chen (2008), Third and fourth Stokes parameters in polarimetric passive microwave remote sensing of rough surfaces over layered media, *Microwave Opt. Technol. Lett.*, *50*(12), 3063–3069, doi:10.1002/mop.23892.

Ulaby, F. T., R. K. Moore, and A. K. Fung (1987), *Microwave Remote Sensing*, Addison-Wesley, Reading, Mass.

Vasavada, A. R., D. A. Paige, and S. E. Wood (1999), Near-surface temperatures on Mercury and the Moon and the stability of polar ice deposits, *Icarus*, *141*(2), 179–193, doi:10.1006/icar.1999.6175.

Wang, Z. Z., Y. Li, J. S. Jiang, et al. (2008), Methods of remote sensing lunar surface by microwave sounder on CE-1, paper presented at the 2008 Int. Conf. Microwave Millimeter Wave Technol., Nanjing, China, 4, 21–24.

Wieczorek, M. A., and S. Huang *(2006)*, *A reanalysis of Apollo 15 and 17 surface and subsurface temperature series, paper presented at Proc.* 37th Lunar Planet. Sci. Conf., Abstract 1682, League City, TX.

Yan, B. K., S. Q. Xiong, *et al. (*2012), Mapping lunar global chemical composition from Chang'E-1 IIM data, *Planet. Space Sci.*, *67*, 119–129, doi:10.1016/j.pss.2012.03.010.

Zheng, Y. C. (2005), Development of lunar soil simulants and characteristics of microwave radiation of lunar regolith, PhD thesis, Graduate University of Chinese Academy of Sciences, Beijing, China.